International Journal of Applied Earth Observations and Geoinformation 108 (2022) 102714

Contents lists available at ScienceDirect

International Journal of Applied Earth Observations and Geoinformation

journal homepage: www.elsevier.com/locate/jag

Global daily gap-free ocean color products from multi-satellite measurements

Xiaoming Liu [a,b,*], Menghua Wang [a]

[a] NOAA Center for Satellite Applications and Research, College Park, MD 20746, USA
[b] CIRA at Colorado State University, Fort Collins, CO 80523, USA

ARTICLE INFO

Keywords:
VIIRS
OLCI
Satellite remote sensing
Global gap-free data
DINEOF
Chlorophyll-a
$K_d(490)$
Suspended particulate matter

ABSTRACT

Gap-free global chlorophyll-a (Chl-a) concentration images derived from the Visible Infrared Imaging Radiometer Suite (VIIRS) onboard the Suomi National Polar-orbiting Partnership (SNPP) and NOAA-20 are now available online in near-real-time for the ocean color community. With the data fusion of Chl-a from the two satellite sources, missing pixels caused by cloud, sun glint contamination, high satellite viewing angles, and other unfavorable conditions are completely filled using the Data Interpolating Empirical Orthogonal Function (DINEOF) method. Our further studies show that adding more data from additional satellite sensors can remarkably improve the spatial coverage of the merged ocean color products, provide more ocean features over coastal and inland waters, and enhance the accuracy of the gap-free data. Since the launch of the Sentinel-3A and Sentinel-3B satellites, the onboard Ocean and Land Colour Instrument (OLCI) sensors have been providing global ocean color product data. In this work, we recruit the OLCI-Sentinel-3A to join the two VIIRS sensors to produce a three-sensor merged ocean color dataset, and further derive global gap-free images using the DINEOF method. It is found that adding OLCI data as the input source significantly enhances the spatial features of high Chl-a by ~10–20% in productive coastal regions and inland lakes. Additionally, the first-ever dataset of global gap-free suspended particulate matter (SPM) and water diffuse attenuation coefficient at 490 nm ($K_d(490)$) is also generated using the three-sensor merged data. Results show that $K_d(490)$ and SPM have similar spatial patterns as that of Chl-a in the major ocean basins, and that SPM can provide more details of the spatial variations than those of $K_d(490)$ in the center of the ocean basin and coastal oceans. Global gap-free Chl-a, $K_d(490)$, and SPM products provide important and useful water quality information particularly over global productive ocean/water regions.

1. Introduction

Satellite ocean color data provide important measurements of optical properties of global oceans and inland waters from space, and have been used to further derive environmental parameters for ocean ecosystem monitoring and ecological/biological oceanography research. The satellite ocean color dataset contains normalized water-leaving radiance $nL_w(\lambda)$ spectra (or remote sensing reflectance $R_{rs}(\lambda)$ spectra) (Gordon and Wang, 1994), chlorophyll-a (Chl-a) concentration (Hu et al., 2012; O'Reilly et al., 1998; Wang and Son, 2016), diffuse attenuation coefficients $K_d(490)$ (i.e., at 490 nm) and $K_d(\mathrm{PAR})$ (i.e., at the photosynthetically available radiation (PAR)) (Son and Wang, 2015; Wang et al., 2009), etc. Chl-a data provide global temporal/spatial distribution and variations of the ocean phytoplankton (or biomass) concentration, and are frequently used to monitor ocean and inland water environments, e.g., ocean/water biological productivity (Behrenfeld and Falkowski, 1997; Platt and Sathyendranath, 1988), harmful algal blooms (HABs) monitoring (Stumpf et al., 2003; Tomlinson et al., 2004; Wang et al., 2021), etc. $K_d(490)$ and $K_d(\mathrm{PAR})$ data have been used for monitoring and studying ocean processes such as phytoplankton photosynthesis and thermal dynamics (Morel and Antoine, 1994; Sathyendranath et al., 1991). Recently, a new satellite algorithm has been developed to routinely derive the suspended particulate matter (SPM) concentration in global waters (Wei et al., 2021; Yu et al., 2019). In fact, SPM data provide primary quantification of water quality and clarity of the world ocean, and have been used for ocean current tracing (Yang et al., 2014), sediment transportation modeling and data assimilation (Ouillon et al., 2004; Stroud et al., 2009), and research on global carbon cycle and

---

[*] Corresponding author.
E-mail address: Xiaoming.Liu@noaa.gov (X. Liu).

https://doi.org/10.1016/j.jag.2022.102714
Received 8 December 2021; Received in revised form 14 January 2022; Accepted 7 February 2022

land–ocean flux (Milliman and Farnsworth, 2013). Currently, $nL_w(\lambda)$, Chl-a, $K_d(490)$, $K_d(\mathrm{PAR})$, and SPM data are being routinely produced from various satellite missions, including the Visible Infrared Imaging Radiometer Suite (VIIRS) (Goldberg et al., 2013) onboard the Suomi National Polar-orbiting Partnership (SNPP) and NOAA-20, and the Ocean and Land Colour Instrument (OLCI) (Donlon et al., 2012) on the Sentinel-3A and Sentinel-3B satellites. In addition, the Moderate Resolution Imaging Spectroradiometer (MODIS) (Esaias et al., 1998), Korean Geostationary Ocean Color Imager (GOCI) (Choi et al., 2012; Wang et al., 2013), and other satellite missions have also provided good quality product data.

However, ocean color daily images from MODIS, VIIRS, OLCI, and other satellite sensors contain a significant amount of invalid pixels because of cloud cover, sun glint contamination, large sensor viewing angle, and other unfavorable conditions (Mikelsons and Wang, 2019). For example, ~70% of missing data exist in global daily images derived from a single VIIRS sensor (Liu and Wang, 2018). Merging images from different satellite missions is an effective way to reduce data gaps in the ocean color images. Overall, a two-sensor merged global daily image contains ~38% more valid pixels than that from a single VIIRS (Liu and Wang, 2019). To completely fill the data gaps in the ocean color images, interpolation methods are needed. Data Interpolating Empirical Orthogonal Functions (DINEOF) is one method that derives a missing value using the spatial and temporal data coherency, and has been effectively used in various satellite ocean remote sensing studies (Alvera-Azcarate et al., 2005; Beckers and Rixen, 2003). In fact, the DINEOF method was compared to other data gap-fill approaches based on the Optimum Interpolation (OI) (Liston and Elder, 2006), Kriging method (Gunes et al., 2006), and Least-Squares-Fit (Stahl et al., 2006), and it was concluded that the DINEOF approach was the most robust technique for satellite remote sensing applications (Henn et al., 2013). The Kriging and Least-Squares-Fit methods are considered to be spatial interpolations, while the DINEOF approach makes use of coherence in temporal and spatial information to infer the missing values. In particular, Henn et al. (2013) found that the DINEOF method was the most accurate and effective method for filling the data gap with long-time durations. Some locations could have cloud cover for several days and even weeks, which causes missing long-time data. For example, there is often persistent cloud cover in the Arabian Sea and Bay of Bengal during the Indian summer monsoon season from May to September. Therefore, we use the DINEOF method to fill the gaps of missing pixels in the daily ocean color image. Indeed, the DINEOF method has been used to routinely generate global gap-free Chl-a data based on merged images derived from two sensors, namely, VIIRS on the SNPP and NOAA-20 satellites (Liu and Wang, 2018, 2019).

Liu and Wang (2019) showed that adding more data from additional satellite sensors to the merged images not only significantly increase the number of valid pixels, but also improves the quality of the derived global gap-free images. Since the launch of the Sentinel-3A/3B satellites in 2016 and 2018, ocean color images from the OLCI sensors have become available. OLCI is a medium-spatial resolution instrument with 21 spectral bands covering wavelengths from the short blue, near-infrared (NIR), and shortwave infrared (SWIR) (Donlon et al., 2012). OLCI has a narrower swath width (1270 km) and higher spatial resolution (300 m) than VIIRS (750 m). Due to differences in sensor spectral response function (SRF), center wavelength, bandwidth, and other sensor characteristics, ocean color data derived from OLCI cannot be directly merged with VIIRS. Wang et al. (2020a) developed a method to obtain ocean color products consistently from multiple satellite sensors. Using this method, the required coefficients for OLCI biological and biogeochemical algorithms can be recalibrated with the in situ hyperspectral radiance measurements from the Marine Optical Buoy (MOBY) in the water off Hawaii (Clark et al., 1997), thereby the OLCI-derived ocean/water property products are consistent with those from VIIRS in open oceans. Therefore, OLCI-measured Chl-a, $K_d(490)$, and SPM can be merged with those from the two VIIRS instruments (Wang et al., 2020a).

In this work, we use ocean color products from three satellites, i.e., two VIIRS sensors and OLCI-Sentinel-3A, to generate a merged Level-3 ocean color dataset, and DINEOF is used to produce Level-4 gap-free Chl-a, $K_d(490)$, and SPM products over global waters. To merge OLCI ocean color data with those from VIIRS, we need to recalibrate the OLCI sensor and reprocess the Level-2 ocean color data using the NOAA ocean color data processing system. It is noted that we are also starting to work on producing OLCI-Sentinel-3B ocean color products using the EUMETSAT reprocessed mission-long Level-1B data. The OLCI-Sentinel-3B ocean color data will be evaluated and added into the multi-sensor merged data stream. The gap-free data reconstructed from three sensors are compared with those from the two VIIRS sensors, as well as from original three-sensor merged data for validation. The remaining content of this paper is constructed as follows: In Section 2, the satellite ocean color data from the three sensors are described, including some details about the data merging and DINEOF methods. Furthermore, the global merged and gap-free Chl-a, $K_d(490)$, and SPM results, their comparisons with two-sensor derived data, and the result of validation against the original data are also documented in Section 3. Finally, we provide the discussions and conclusion in Section 4.

2. Data and methods

2.1. Satellite ocean color data

The Multi-Sensor Level-1 to Level-2 (MSL12) is the NOAA official enterprise VIIRS ocean color data processing system, including VIIRS on all the future Joint Polar Satellite System (JPSS) missions. MSL12 can also be used for processing satellite data for OLCI on Sentinel-3A and Sentinel-3B. As it was initially designed, MSL12 has the capability to produce ocean color products consistently for various sensors (Wang et al., 2002). Using the Level-1B data as input, MSL12 generates ocean color Level-2 product data, including $nL_w(\lambda)$, Chl-a, $K_d(490)$, $K_d(\mathrm{PAR})$, and SPM, etc. In addition, MSL12 provides options for using various atmospheric correction algorithms, including the NIR-, SWIR-, and NIR-SWIR-based algorithms (Gordon and Wang, 1994; Jiang and Wang, 2014; Wang, 2007; Wang and Shi, 2007). The SWIR-based algorithm was developed to make accurate ocean color measurements in global highly turbid waters. Indeed, it has been shown in several previous studies that the NIR-SWIR-based ocean color products are of a better quality over global open oceans and turbid coastal/inland waters (Shi and Wang, 2012, 2014; Shi et al., 2011). It is noted that there have been significant efforts to evaluate and validate satellite-derived ocean color products using in situ data and other approaches (e.g., statistical analysis) (Barnes et al., 2019; Hlaing et al., 2013; Hu et al., 2020; Mikelsons et al., 2020; Wang et al., 2020b). In particular, VIIRS ocean color products are being well evaluated by the NOAA ocean color team and NOAA VIIRS ocean color calibration/validation (Cal/Val) team, including annual dedicated ocean color Cal/Val cruises since 2014, which are documented in the NOAA five cruise reports, e.g., one most recent report (Ondrusek et al., 2021).

In this work, we use the MSL12-derived Chl-a, $K_d(490)$, and SPM data (derived from $nL_w(\lambda)$ spectra) from VIIRS and OLCI. The Chl-a algorithm uses the ocean color index (OCI) method, which has been proven to be more stable and accurate for clear (low Chl-a) oceans (Wang and Son, 2016). The $K_d(490)$ algorithm is a hybrid of the clear ocean (standard) model (Mueller, 2000) and the turbid water model, so that $K_d(490)$ data for both clear and productive oceans/waters can be accurately retrieved (Wang et al., 2009). The SPM algorithm utilizes input from satellite-measured $R_{rs}(\lambda)$ spectra at the NIR, red, green, and blue (NIR-RGB), and also combines algorithms for both turbid and clear waters for global ocean data retrievals (Wei et al., 2021; Yu et al., 2019). Satellite-retrieved SPM data directly measure the amount of both organic and inorganic suspended particles in the upper water layers. In fact, over the coastal and inland waters, SPM are mainly sediments from shoreline erosion, river discharge, and bottom resuspension (Wei et al., 2021; Yu et al., 2019). On the other hand, suspended biogenic particles are dominant in the upper layers over open oceans (Wei et al., 2021).

The Level-2 data are spatially and temporally binned to generate the global Level-3 ocean color products of Chl-a, $K_d(490)$, and SPM (Campbell et al., 1996). The Level-3 files employ the equal-area sinusoidal projection, which has significantly fewer grids in the high-latitude regions than regular projections, such as a cylindrical or Mercator projection. This advantage significantly benefits the process of generating global gap-free ocean color products with a better computation performance in near-real-time settings. To ensure high quality Level-3 data, prior to the binning process, some important MSL12-generated Level-2 data quality masks and flags, e.g., masks for land and cloud, flags for cloud shadow and straylight, high sun glint, large solar and satellite viewing angles, etc., are applied to remove substandard quality data in Level-2 files (Jiang and Wang, 2013; Mikelsons et al., 2020; Mikelsons et al., 2021).

It is noted that VIIRS data on SNPP and NOAA-20 have been available from December 2011 and November 2017, respectively, and OLCI data on Sentinel-3A and Sentinel-3B have been available from February 2016 and April 2018, respectively. Both VIIRS sensors are on orbit with equatorial crossing at around 1:30 p.m. (ascending node), while the two OLCI sensors are at descending node with equatorial crossing at around 10:00 a.m. VIIRS has a swath width of about 3040 km with 750 m spatial resolution at nadir, while an OLCI has a narrower swath (1270 km) with a higher spatial resolution (300 m). Due to cloud, high sun-glint contamination, high solar- and/or sensor-zenith angles, etc., a daily global VIIRS image has ~ 70% missing pixels, while a daily global OLCI image has ~ 80% missing pixels. The higher amount of daily missing data for OLCI is mainly due to a narrower OLCI data swath width as compared to that from VIIRS.

2.2. Merging ocean color satellite data from three sensors

We include ocean color data derived from OLCI-Sentinel-3A with the two VIIRS sensors to produce a three-sensor merged global ocean color dataset. As mentioned previously, the SRF effects on the satellite products (e.g., Chl-a, $K_d(490)$, and SPM) derived from the three sensors are specifically accounted for over open oceans using the Wang et al. (2020a) approach. There are differences in sensor spectral characteristics from different satellite sensors even for the same satellite series that is designed to have the same sensor spectral characteristics (Wang et al., 2020a). To account for the SRF effects on the satellite-derived biological and biogeochemical products, e.g., Chl-a, $K_d(490)$, SPM, etc., these algorithms are modified based on the specific SRF for providing consistent ocean color products using in situ hyperspectral MOBY $nL_w(\lambda)$ measurements applicable for global open oceans (Wang et al., 2020a). Therefore, Chl-a, $K_d(490)$, and SPM derived from the three sensors are generally consistent over open oceans and can be merged seamlessly without further adjustment for generating three-sensor merged products. Over turbid coastal and inland waters, however, the spectral $nL_w(\lambda)$ relationships with water biological and biogeochemical properties are usually location dependent (Shi and Wang, 2014). In addition, uncertainties from satellite biological and biogeochemical algorithms are generally much larger than those from the effect of SRF differences. Therefore, no algorithm adjustments are made for the three sensors over turbid coastal and inland waters (Wang et al., 2020a). As described in the methodology of merging two VIIRS-measured ocean color data (Liu and Wang, 2019), the weighted averages of the Level-3 bins for the three-sensor ocean color data are calculated as merged products, and the number of valid data in each bin is used as the weight (Campbell et al., 1996).

2.3. The DINEOF method

The DINEOF approach for filling data gaps is essentially based on the Empirical Orthogonal Function (EOF) method, and it uses the dominant spatial patterns (EOF modes) extracted from a data time series to reconstruct the missing data (Alvera-Azcarate et al., 2005; Beckers and Rixen, 2003). A simplified description of the DINEOF procedure can also be found in Liu and Wang (2018). We use the DINEOF method to recalculate and fill the missing data gaps from the three-sensor merged Chl-a, $K_d(490)$, and SPM data. Specifically, we apply the DINEOF method directly to the three-sensor merged global Level-3 files, rather than mapped files. In addition, the global Level-3 (three-sensor merged) dataset is partitioned into sixteen zonal sections (each with 10°-zone) from 80°S–80°N, thereby the sixteen-zonal data sections can be processed simultaneously to further improve the computation performance.

In our experiment, we use global daily Level-3 data from the previous 29 days to fill the data gaps in the image of a specific date. Therefore, for each DINEOF process, a 30-day time series of daily data is used as input, and the output is the gap-free data of the last day. In an operational setting, this procedure can be applied to a rolling 30-day time series to gap-fill the most recent daily image in near-real-time. We briefly describe the DINEOF procedure to reconstruct missing pixels as follows:

(1) Store the original dataset in a two-dimensional spatio-temporal matrix (the first dimension is the number of grids in the spatial domain, and the second dimension is the number of time steps in the time series).
(2) Remove the temporal and spatial mean from the data, and set zeroes to all missing values.
(3) Calculate the first EOF mode, and replace the missing values with the initial guess using only the first EOF mode.
(4) Iteratively recalculate the first EOF mode using the previous best guess as the initial value of the missing data for the subsequent iteration until the process converges (threshold $= 10^{-8}$).
(5) Subsequently, repeat steps 3 and 4 for the second, third, fourth, EOF mode, and use a cross-validation technique (Beckers and Rixen, 2003) to determine the optimal number of EOF modes.
(6) Finally, reconstruct missing pixels using the optimal number of EOF modes.

It should be noted that not all EOF modes are used in the final data reconstruction, and the noise, as well as small scale and transient features in the high order EOF modes, are removed from the reconstructed data. The process to determine the optimum number of EOF modes in the final reconstruction is fully automatic. However, in the parameter file, we need set the maximum number of EOF modes to the temporal size (=30 for this study), so that it calculates enough number of EOF modes before the optimum number of EOF modes is reached. To quantitatively evaluate the accuracy of the DINEOF data reconstruction method, a set of valid pixels are intentionally treated as “missing pixels,” so that DINEOF-reconstructed data can be compared with the original data. Specifically, before the DINEOF process, 5% of the valid (non-missing) pixels are purposely removed from the original global data. The locations of these validation pixels are randomly selected using the random number generator. After the DINEOF process, these data are reconstructed and compared with those from the original data set.

3. Results

Since the two-sensor gap-free Chl-a data are routinely produced, we focused on comparing the three-sensor gap-free Chl-a data with those from the two-sensor. For $K_d(490)$ and SPM data, it is the first time that we produce the gap-free data, and there are no two-sensor gap-free data for comparison. For these two parameters, we followed the validation procedure described in Section 2.3 to validate the products with those from the original data sets.

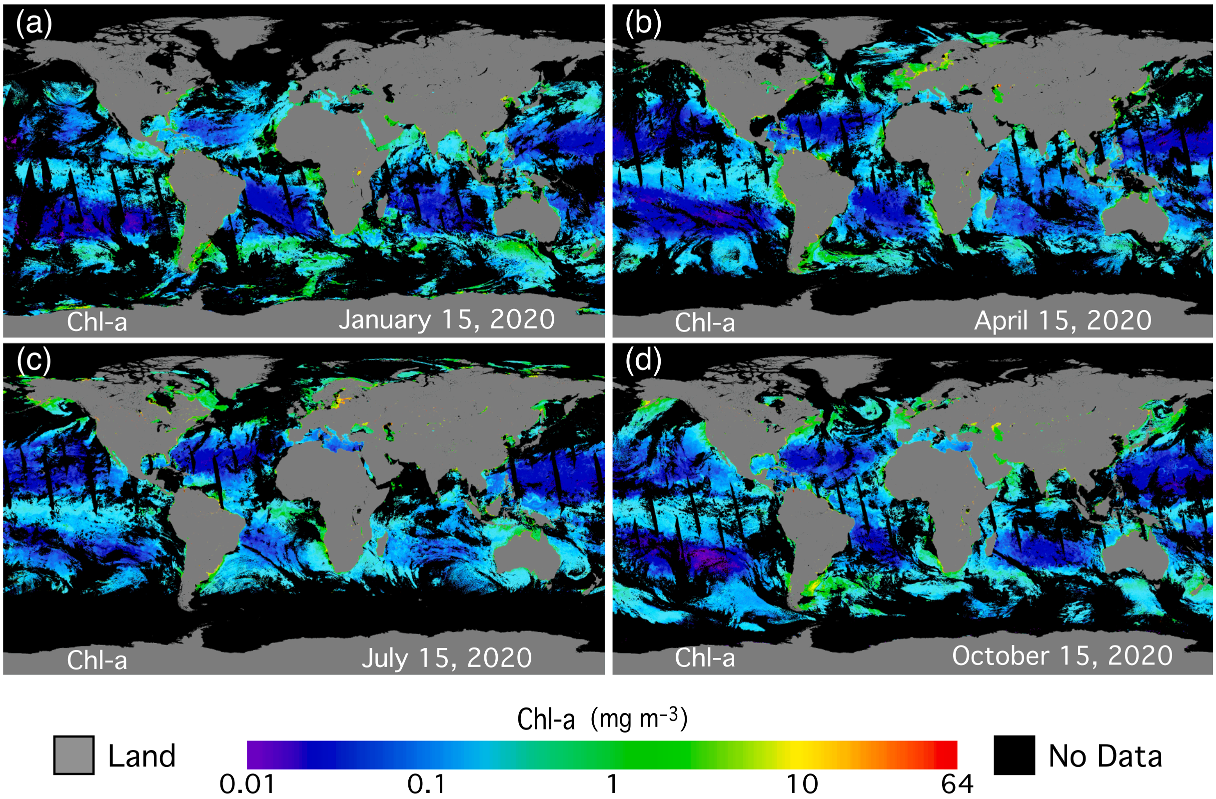

Fig. 1. Three-sensor merged Chl-a concentration from VIIRS-SNPP, VIIRS-NOAA-20, and OLCI-Sentinel-3A on (a) January 15, (b) April 15, (c) July 15, and (d) October 15, 2020.

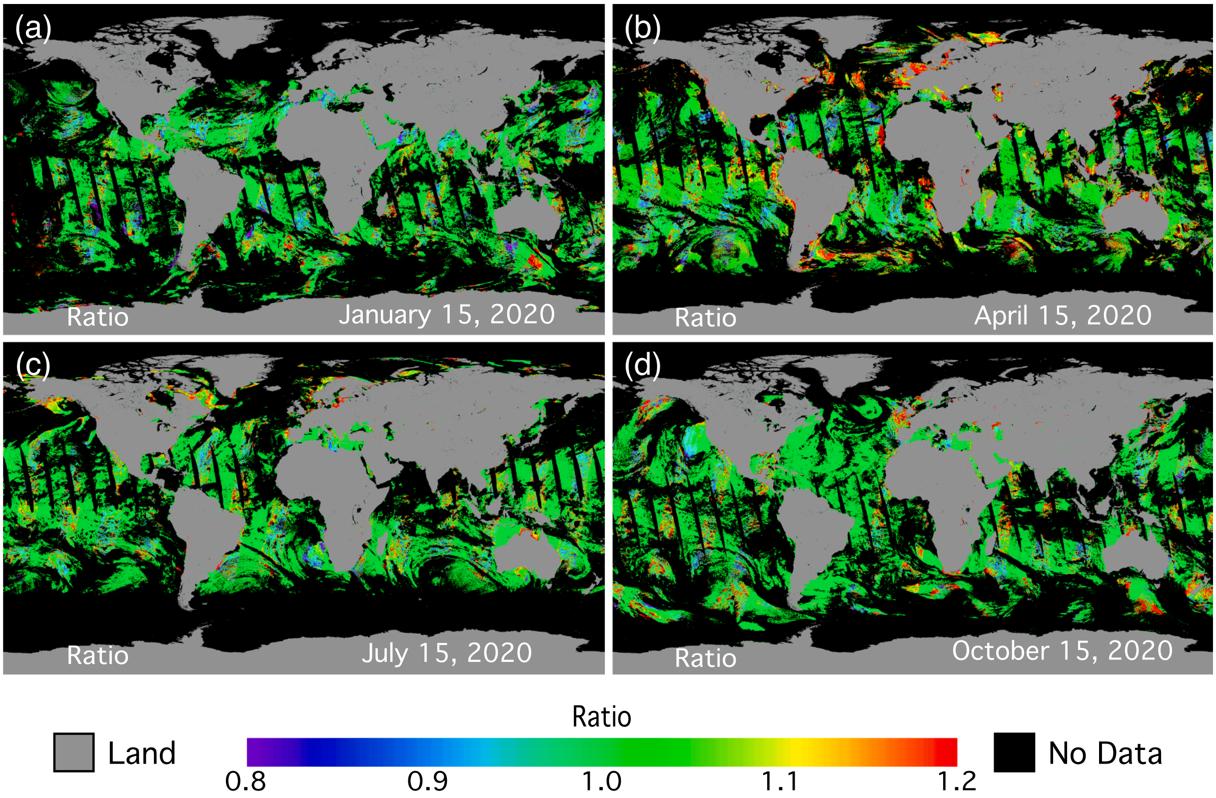

Fig. 2. Global *Chl-a*$^{(3\text{-}Sens)}$/*Chl-a*$^{(2\text{-}Sens)}$ ratio image on (a) January 15, (b) April 15, (c) July 15, and (d) October 15, 2020. *Chl-a*$^{(3\text{-}Sens)}$ are merged Chl-a from three sensors (VIIRS-SNPP, VIIRS-NOAA-20, and OLCI-Sentinel-3A) and *Chl-a*$^{(2\text{-}Sens)}$ are merged Chl-a from the two VIIRS sensors.

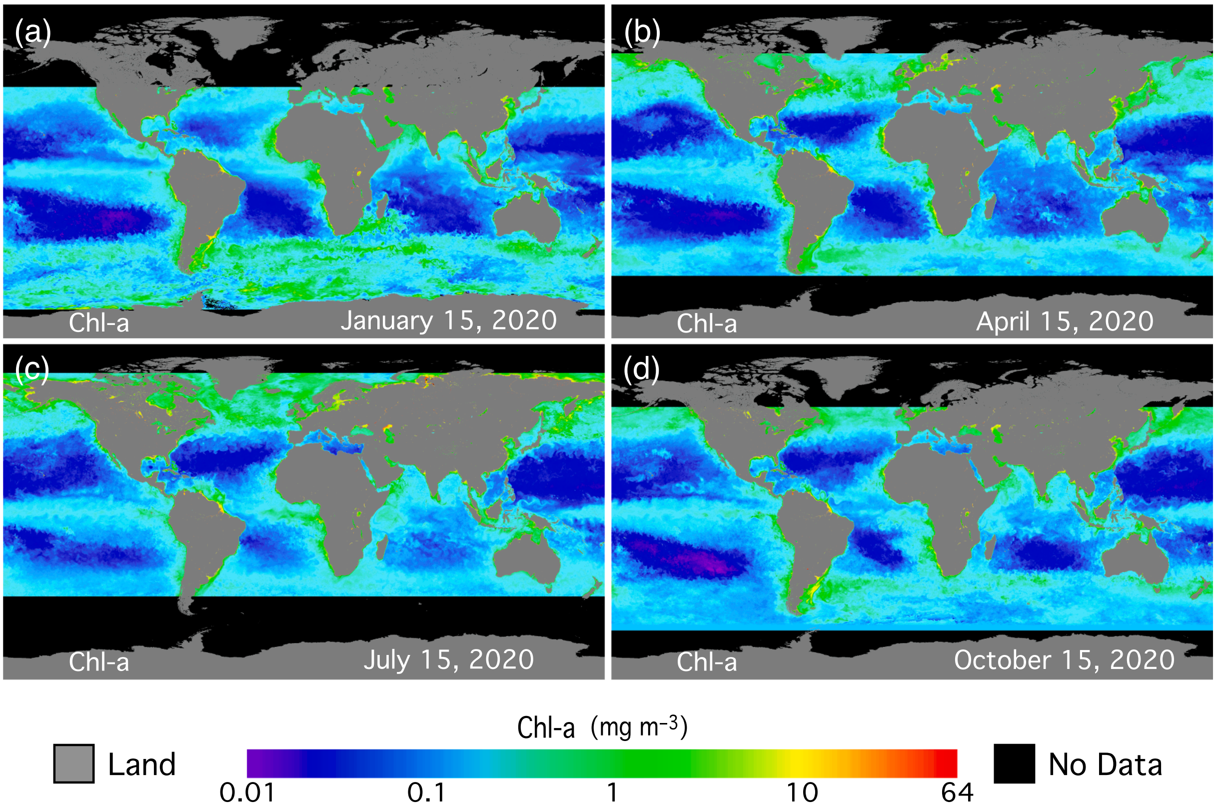

Fig. 3. Global gap-free Chl-a concentration reconstructed from three sensors (VIIRS-SNPP, VIIRS-NOAA-20, and OLCI-Sentinel-3A) on (a) January 15, (b) April 15, (c) July 15, and (d) October 15, 2020.

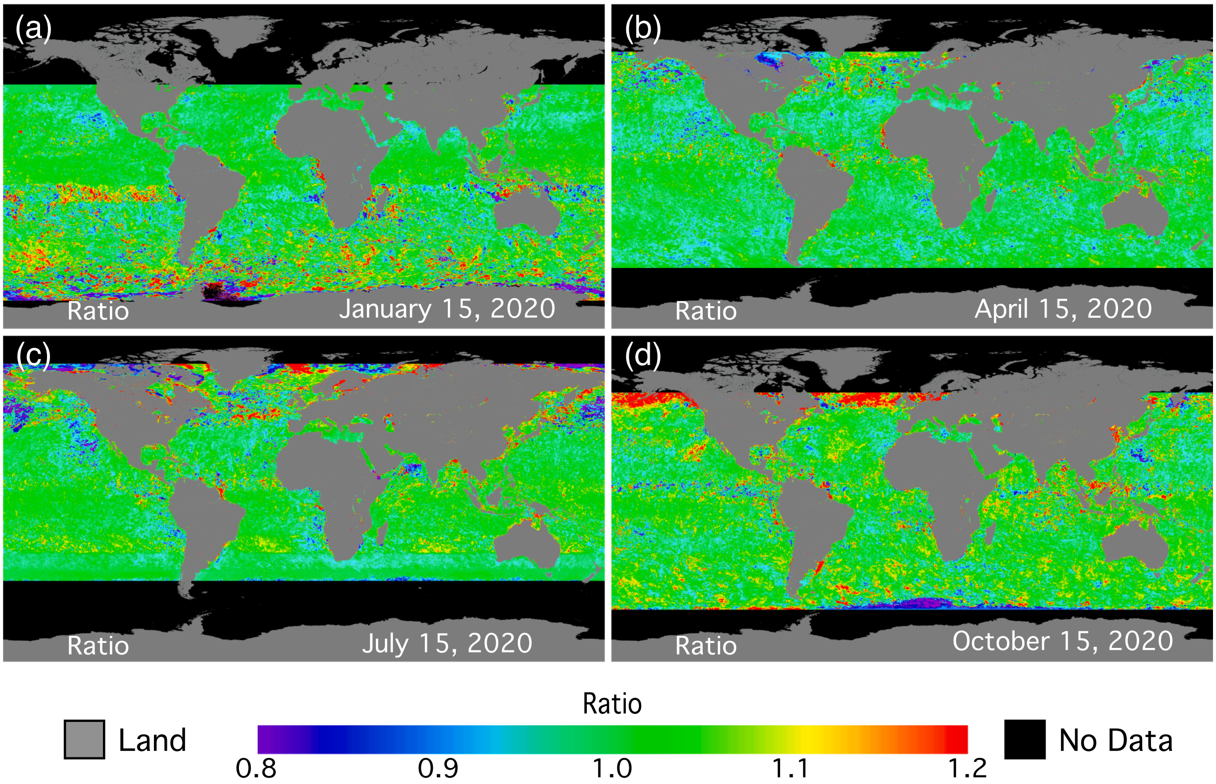

Fig. 4. Global gap-free *Chl-a*$^{(3\text{-}Sens)}$/*Chl-a*$^{(2\text{-}Sens)}$ ratio image on (a) January 15, (b) April 15, (c) July 15, and (d) October 15, 2020. *Chl-a*$^{(3\text{-}Sens)}$ are gap-free Chl-a reconstructed from three sensors (VIIRS-SNPP, VIIRS-NOAA-20, and OLCI-Sentinel-3A) and *Chl-a*$^{(2\text{-}Sens)}$ are gap-free Chl-a from the two VIIRS sensors.

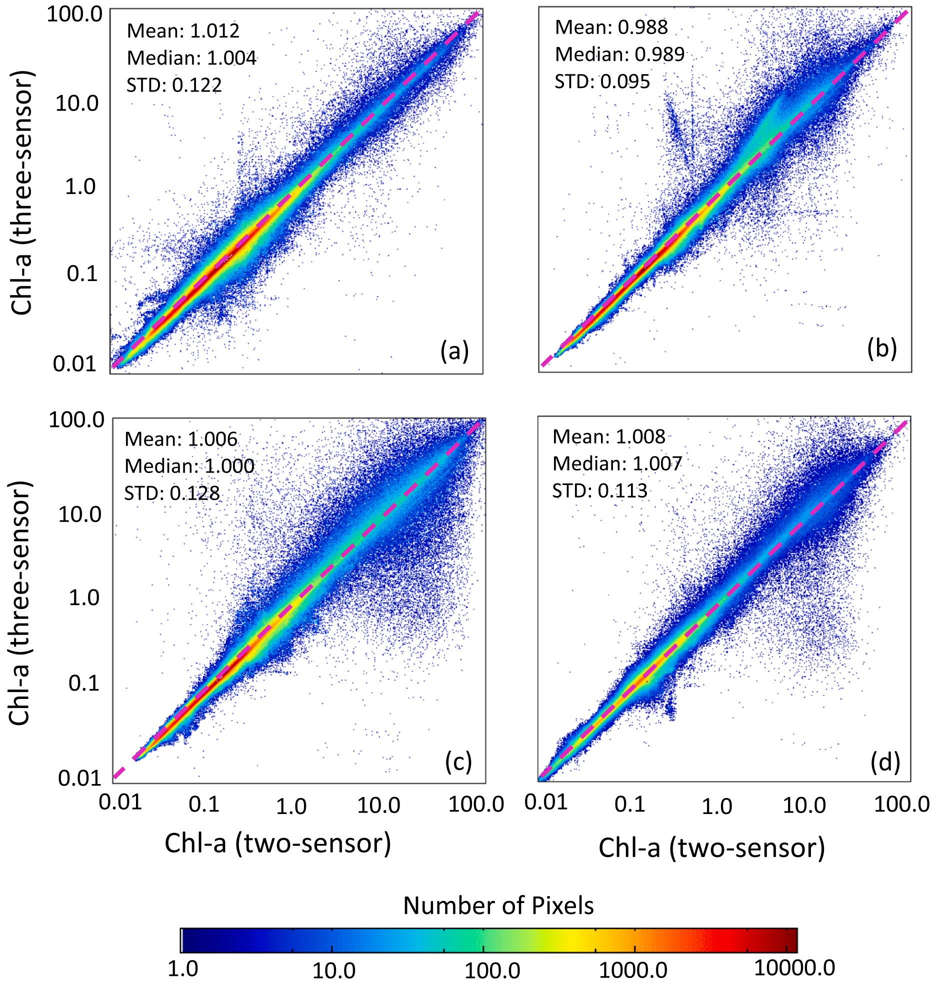

Fig. 5. Density scatter plots of gap-free *Chl-a*$^{(3\text{-}Sens)}$ versus *Chl-a*$^{(2\text{-}Sens)}$ on (a) January 15, (b) April 15, (c) July 15, and (d) October 15, 2020. *Chl-a*$^{(3\text{-}Sens)}$ are gap-free Chl-a reconstructed from three sensors (VIIRS-SNPP, VIIRS-NOAA-20, and OLCI-Sentinel-3A) and *Chl-a*$^{(2\text{-}Sens)}$ are gap-free Chl-a from the two VIIRS sensors. Note that Chl-a unit is mg m^{-3}.

Table 1
Statistics of ratio (*Chl-a*$^{(3\text{-}Sens)}$/*Chl-a*$^{(2\text{-}Sens)}$) and difference (Diff.), i.e., (*Chl-a*$^{(3\text{-}Sens)}$−*Chl-a*$^{(2\text{-}Sens)}$), for the months of January, April, July, and October in 2020 over various global ocean/water regions derived from global monthly (daily) data.

Month (in 2020)		January		April		July		October	
		Ratio	Diff.[†]	Ratio	Diff.[†]	Ratio	Diff.[†]	Ratio	Diff.[†]
Global Waters	Mean	1.017	0.013	0.998	−0.003	1.001	0.031	1.014	0.019
	Median	1.006	0.001	0.995	0.000	0.996	0.000	1.009	0.001
	STD	0.145	0.418	0.117	0.590	0.127	0.861	0.114	0.562
Deep Waters	Mean	1.018	0.003	0.998	−0.005	0.995	0.006	1.012	0.005
	Median	1.007	0.001	0.995	0.000	0.994	0.000	1.008	0.001
	STD	0.133	0.155	0.101	0.202	0.099	0.428	0.102	0.290
Oligotrophic Waters	Mean	0.999	−0.003	0.985	−0.013	0.990	0.011	1.007	0.007
	Median	0.992	0.000	0.986	0.000	0.990	0.000	1.001	0.000
	STD	0.097	0.187	0.097	0.321	0.107	0.661	0.087	0.506
Coastal/Inland Waters	Mean	1.015	0.092	0.991	−0.002	1.026	0.155	1.054	0.156
	Median	1.005	0.003	0.991	−0.001	1.022	0.012	1.038	0.015
	STD	0.193	1.246	0.228	1.588	0.230	1.931	0.198	1.645

[†] Unit of mg m^{-3}.

3.1. Three-sensor Chl-a data

For convenience in description and discussion below, we define *Chl-a*$^{(3\text{-}Sens)}$ as Chl-a data derived from the three sensors, and similarly *Chl-a*$^{(2\text{-}Sens)}$ as for Chl-a derived from two VIIRS sensors.

3.1.1. Three-sensor merged daily global Chl-a data

Fig. 1 provides examples of the global *Chl-a*$^{(3\text{-}Sens)}$ merged images on January 15, April 15, July 15, and October 15 in 2020, covering four days in four seasons. Although the swath of OLCI is much narrower than VIIRS, adding OLCI ocean color data to the *Chl-a*$^{(2\text{-}Sens)}$ merged images significantly reduced the number of missing pixels because of cloud,

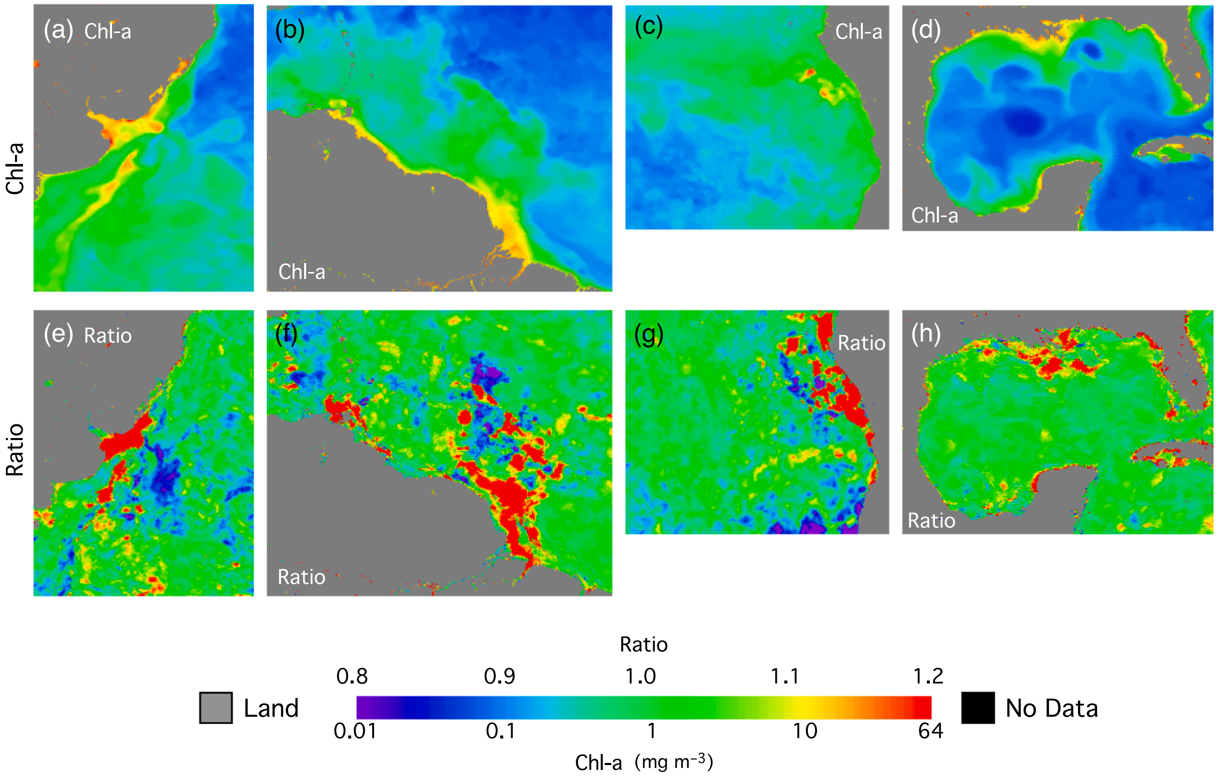

Fig. 6. Gap-free Chl-a reconstructed from three sensors (VIIRS-SNPP, VIIRS-NOAA-20, and OLCI-Sentinel-3A) in the coastal region of (a) La Plata River Estuary on January 15, 2020, (b) Brazil Coast on July 15, 2020, (c) Southwest Africa Coast on July 15, 2020, and (d) Gulf of Mexico on July 15, 2020. The corresponding $Chl\text{-}a^{(3\text{-}Sens)}/Chl\text{-}a^{(2\text{-}Sens)}$ ratio images for cases (a)–(d) are shown in panels (e)–(h), respectively.

Table 2
Statistics of ratio ($Chl\text{-}a^{(3\text{-}Sens)}/Chl\text{-}a^{(2\text{-}Sens)}$) and difference ($Chl\text{-}a^{(3\text{-}Sens)} - Chl\text{-}a^{(2\text{-}Sens)}$) for the four months of January, April, July, and October in 2020 over the six coastal regions of the Gulf of Mexico, U.S. East Coast, U.S. West Coast, Brazil Coast, Bay of Bangel, and China East Coast.

Region	Ratio			Difference (mg m^{-3})		
	Mean	Median	STD	Mean	Median	STD
Gulf of Mexico	1.019	1.005	0.126	0.104	0.001	0.995
U.S. East Coast	1.008	0.999	0.149	0.104	0.000	1.137
U.S. West Coast	0.981	0.978	0.111	0.043	−0.003	0.689
Brazil Coast	1.022	1.011	0.120	0.046	0.001	0.801
Bay of Bangel	1.018	1.010	0.115	0.016	0.002	0.631
China East Coast	1.056	1.042	0.173	0.234	0.054	1.288

large sensor (viewing) angles, and high sun glint contamination. On average, a global daily $Chl\text{-}a^{(3\text{-}Sens)}$ image from the three-sensor has ~11% more valid pixels than that from the two-sensor $Chl\text{-}a^{(2\text{-}Sens)}$ image. Specifically, on January 15 (Fig. 1a), the data gaps from the large satellite viewing angle and high sun-glint were mainly located in the South Pacific, South Atlantic, and South Indian Oceans, and OLCI data can partially or completely fill the data gaps. On July 15 (Fig. 1c), similar data gaps were also reduced in the North Pacific and North Atlantic Oceans. On April 15 and October 15 (Fig. 1b and d), the large satellite viewing angle and high sun-glint data gaps were located in the tropical oceans near the equator, and they were partially filled with OLCI data. In addition, the Sentinel-3A orbit has equator crossing around 10:00 local time (descending), while the SNPP/NOAA-20 orbit around 13:30 local time (ascending). The difference in cloud coverage at different times of the satellite passing in the region also reduces the number of missing pixels from the three-sensor merged data.

To compare the three-sensor merged data with those from the two-sensor, Fig. 2 shows the image of $Chl\text{-}a^{(3\text{-}Sens)}/Chl\text{-}a^{(2\text{-}Sens)}$ ratio on the same four days as in Fig. 1. For most of the areas in the open ocean, ratios of $Chl\text{-}a^{(3\text{-}Sens)}/Chl\text{-}a^{(2\text{-}Sens)}$ are close to 1.0 (green color), which indicates that the three-sensor merged $Chl\text{-}a^{(3\text{-}Sens)}$ data are close to those from the two-sensor $Chl\text{-}a^{(2\text{-}Sens)}$. However, in some high latitude areas and over turbid coastal/inland waters, ratios of $Chl\text{-}a^{(3\text{-}Sens)}/Chl\text{-}a^{(2\text{-}Sens)}$ are different from the unity, which are mostly attributed to the difference in coverage between the VIIRS and OLCI measurements. For example, even at the 50°N latitude ocean regions, during the winter to spring season, the solar-zenith angle could reach to ~60°–70°, which is close to the limitation of 70° for ocean color data processing.

3.1.2. *Global gap-free Chl-a data*

Fig. 3 provides examples of the global daily gap-free $Chl\text{-}a^{(3\text{-}Sens)}$ images on January 15, April 15, July 15, and October 15 in 2020. Similar to daily gap-free $Chl\text{-}a^{(2\text{-}Sens)}$ images reconstructed from two VIIRS sensors (Liu and Wang, 2019), the low Chl-a (<0.1 mg m^{-3}) are mainly found in the five subtropical ocean gyres, i.e., the north and south Pacific, north and south Atlantic, and south Indian Oceans. For these global oligotrophic waters, Chl-a have two peaks annually, both in the winter season (boreal and Australian winters) (Wang et al., 2021), due primarily to the winter strong vertical mixing (Signorini et al., 2015). In the equatorial Pacific and Atlantic, the easterly trade winds blow along the equator and waters are transported away from the equator on both its north and south side (Gill, 1982). The divergence of the surface flow induces an upwelling of the cold and nutrient-rich waters and creates a productive phytoplankton bloom zone, so that Chl-a (ranging ~0.1–1.0 mg m^{-3}) are higher than those in the subtropical gyres. Over the high latitude ocean region, surface water is cold with less vertical density gradient, and the vertical mixing of water can reach to depths much greater than euphotic zone (Siegel et al., 2002). As a result, with sufficient nutrient supply due to vertical mixing, high Chl-a (> 1.0 mg m^{-3}) are present in the high-latitude oceans of the Northern Atlantic, Northern Pacific, and the Southern Ocean. We also found a

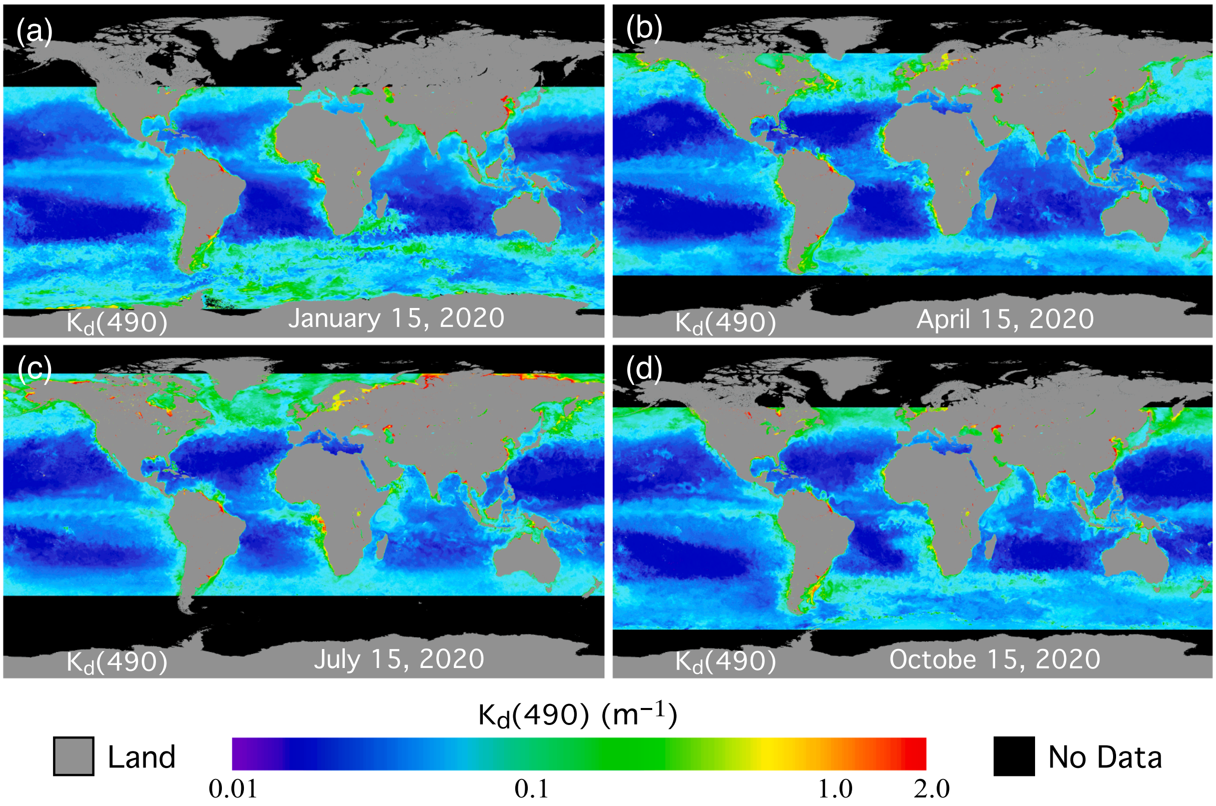

Fig. 7. Global gap-free K_d(490) reconstructed from three sensors (VIIRS-SNPP, VIIRS-NOAA-20, and OLCI-Sentinel-3A) on (a) January 15, (b) April 15, (c) July 15, and (d) October 15, 2020.

seasonal trend of Chl-a variation in the high-latitude ocean regions: the Southern Ocean has a maximum Chl-a in January, while Chl-a in the Northern Atlantic and Northern Pacific have a maximum in July (Boss and Behrenfeld, 2010). In coastal oceans, nutrient sources from land, resuspension from sea floor, and coastal upwelling support high biological productivity (Shi and Wang, 2012). Indeed, there are significantly high Chl-a ($>$ 1.0 mg m^{-3}) on the West Africa Coast, South America coast, Arabian Sea and Bay of Bangle, and China East Coast.

Since the global gap-free *Chl-a*$^{(2\text{-}Sens)}$ data have already been validated (Liu and Wang, 2019), we compare the gap-free *Chl-a*$^{(3\text{-}Sens)}$ and *Chl-a*$^{(2\text{-}Sens)}$ images for evaluations. The images of the gap-free *Chl-a*$^{(3\text{-}Sens)}$/*Chl-a*$^{(2\text{-}Sens)}$ ratio on the same four days as in Fig. 3 are provided in Fig. 4. Results show that ratios in *Chl-a*$^{(3\text{-}Sens)}$/*Chl-a*$^{(2\text{-}Sens)}$ are close to 1.0 in most pixels (green color). However, there is significant noise in the Southern Ocean and equatorial ocean in the image on January 15 (Fig. 4a), and in the northern Atlantic and Pacific Oceans on July 15 (Fig. 4c). In comparison, there is less noise in images of April 15 and October 15 (Fig. 4b and d). For quantitative evaluations, Fig. 5 provides the density-scatter plot of *Chl-a*$^{(3\text{-}Sens)}$ (three-sensor) versus *Chl-a*$^{(2\text{-}Sens)}$ (two-sensor) gap-free images on the same four days as in Fig. 3. We can see that the density-scatter plots are closer to 1:1 line in all images for the four-daily data, while there are slightly more scatters (noise) for the cases of January 15 and July 15. Quantitatively, the standard deviation (STD) values of the *Chl-a*$^{(3\text{-}Sens)}$/*Chl-a*$^{(2\text{-}Sens)}$ ratio are 0.122, 0.095, 0.128, and 0.113 for the cases of January 15, April 15, July 15, and October 15, respectively, reflecting high noise data for both January 15 and July 15 cases as shown in Fig. 4.

For accurately characterizing the seasonal effect, Table 1 provides the statistics of the monthly averaged ratio (*Chl-a*$^{(3\text{-}Sens)}$/*Chl-a*$^{(2\text{-}Sens)}$) and difference (*Chl-a*$^{(3\text{-}Sens)}$ − *Chl-a*$^{(2\text{-}Sens)}$) in January, April, July, and October 2020 for global waters, global deep waters (depth $>$ 1 km), global oligotrophic waters (Chl-a $\leq \sim$0.1 mg m^{-3}), and global coastal/inland waters (i.e., depth $\leq$ 1 km). Note that the monthly statistics data were derived from the entire month (daily) data for these four months. Results in Table 1 show that *Chl-a*$^{(3\text{-}Sens)}$ are very close to *Chl-a*$^{(2\text{-}Sens)}$ in global oligotrophic waters for the four months with a *Chl-a*$^{(3\text{-}Sens)}$/*Chl-a*$^{(2\text{-}Sens)}$ ratio that varies from 0.985 to 1.007, and a difference that varies from −0.013 to 0.011 mg m^{-3}. However, over global coastal and inland waters, the three-sensor *Chl-a*$^{(3\text{-}Sens)}$ are usually slightly higher than the two-sensor *Chl-a*$^{(2\text{-}Sens)}$ with additionally larger STD values, i.e., Chl-a ratios vary from 0.991 to 1.054, and Chl-a differences are quite significant from −0.002 to 0.156 mg m^{-3}. This is mainly attributed to the difference between Chl-a data derived from VIIRS and OLCI in coastal and inland waters. Chl-a derived from three sensors are usually different over turbid coastal and inland waters due to the Chl-a algorithm performance issue, as well as differences with the SRF effect on the Chl-a algorithm. However, the gap-free Chl-a spatial features derived from the three-sensor merged data are quite useful over coastal and inland water. Overall, over global waters, *Chl-a*$^{(3\text{-}Sens)}$ are more or less consistent with *Chl-a*$^{(2\text{-}Sens)}$, i.e., the mean ratio varies from 0.998 to 1.017, and the median ratio from 0.995 to 1.009.

The monthly means of the *Chl-a*$^{(3\text{-}Sens)}$/*Chl-a*$^{(2\text{-}Sens)}$ ratio also show seasonal variations. In global oceans, *Chl-a*$^{(3\text{-}Sens)}$ data are very close to *Chl-a*$^{(2\text{-}Sens)}$ in April and July, while *Chl-a*$^{(3\text{-}Sens)}$ data are ~1.5% higher than the *Chl-a*$^{(2\text{-}Sens)}$ data in January and October. Over global oligotrophic waters, *Chl-a*$^{(3\text{-}Sens)}$ data are smaller than *Chl-a*$^{(2\text{-}Sens)}$ in April and July (mean *Chl-a*$^{(3\text{-}Sens)}$/*Chl-a*$^{(2\text{-}Sens)}$ ratios are 0.985 and 0.990), while they are very close in January and October.

3.1.3. *Gap-free Chl-a in coastal oceans*

Fig. 6 provides examples of *Chl-a*$^{(3\text{-}Sens)}$ images in the coastal regions near the La Plata River Estuary (Fig. 6a), Amazon River Estuary (Fig. 6b), West Africa Coast (Fig. 6c), and Gulf of Mexico (Fig. 6d). The La Plata River Estuary and its vicinity is one of the most extremely turbid coastal oceans, and Chl-a are high due to the nutrient input from river discharge (Shi and Wang, 2020). Fig. 6a shows the gap-free *Chl-a*$^{(3\text{-}Sens)}$

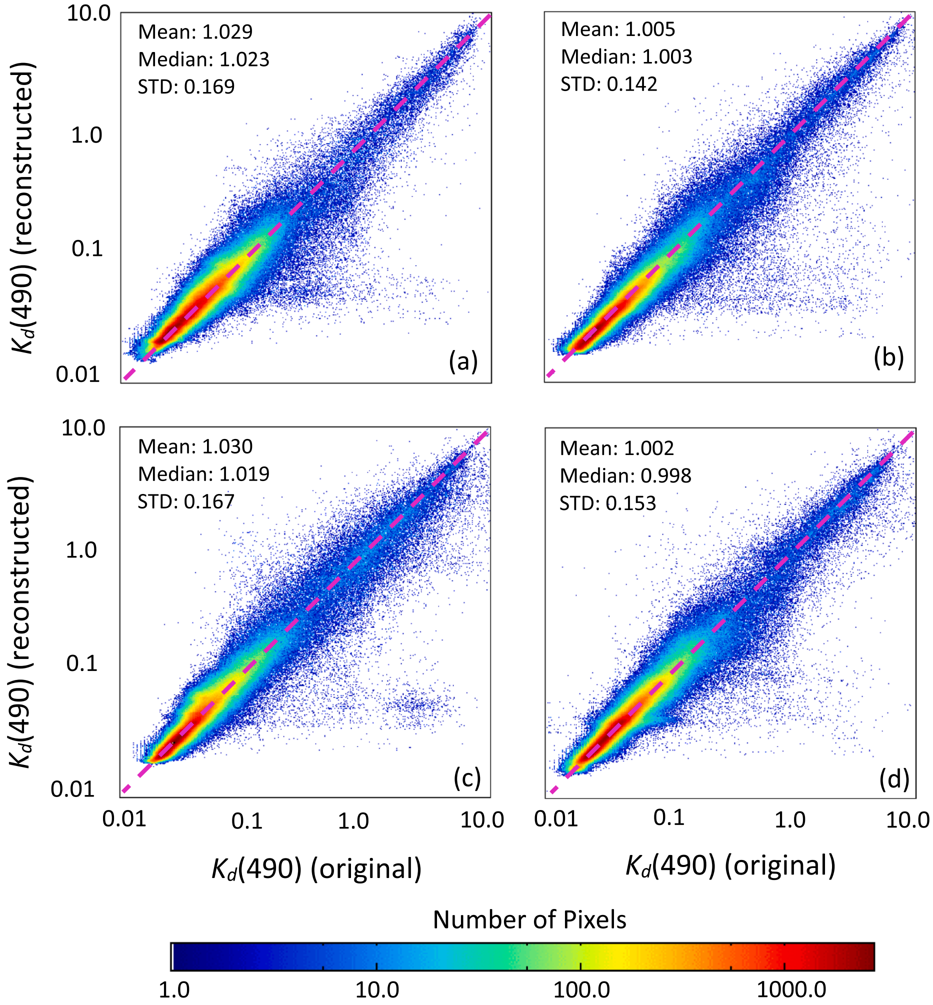

Fig. 8. Density scatter plots of gap-free K_d(490) versus original K_d(490) on (a) January 15, (b) April 15, (c) July 15, and (d) October 15, 2020. Note that K_d(490) unit is m^{-1}.

image on January 15, 2020, near the La Plata River Estuary. The high Chl-a features (> ~10 mg m^{-3}) were found inside the estuary and in coastal eddies. Fig. 6e shows the image of the *Chl-a*$^{(3\text{-}Sens)}$/*Chl-a*$^{(2\text{-}Sens)}$ ratio, and the variation of the ratio was quite significant across the region. In the areas of significantly large Chl-a (> ~10 mg m^{-3}), *Chl-a*$^{(3\text{-}Sens)}$ values were ~10–20% higher than *Chl-a*$^{(2\text{-}Sens)}$ values, indicating that these spatial features of high Chl-a were significantly enhanced by adding the OLCI data as an input source.

Similarly, we also found high Chl-a features in the *Chl-a*$^{(3\text{-}Sens)}$ image near the Amazon River Estuary and North Brazil Current (NBC) on July 15, 2020 (Fig. 6b). Chl-a in the Amazon River Estuary were quite high (~10 mg m^{-3}) due to nutrients in river runoff. As a western boundary current, the NBC flows northward along the coast of Brazil (Johns et al., 1990). High nutrient water exported from the Amazon River significantly enhances the biological activities in the NBC. The NBC separates from the Brazil Coast near 7°N and sometimes curves back to pinch off large warm-core rings (Fratantoni and Glickson, 2002). *Chl-a*$^{(3\text{-}Sens)}$ in NBC and its associated ring were ~1.0 mg m^{-3} (Fig. 6b). Results in Fig. 6f show that the spatial features of high Chl-a in the Amazon River Estuary and the NBC ring were significantly enhanced using the three-sensor *Chl-a*$^{(3\text{-}Sens)}$ data.

Fig. 6c shows *Chl-a*$^{(3\text{-}Sens)}$ along the southwest coast of Africa on July 15, 2020. The southwest coast of Africa is known for its upwelling including the Benguela Current upwelling system, driven by the Ekman-pumping related to the alongshore wind-stress (Kämpf and Chapman, 2016). In addition, the Congo River also brings significant nutrient supply into the coastal waters and stimulates phytoplankton blooms (Hardman-Mountford et al., 2003). Chl-a data in the southwest coast of Africa are generally > ~1.0 mg m^{-3}. From Fig. 6g, it can be seen that in the areas of coastal upwelling, *Chl-a*$^{(3\text{-}Sens)}$/*Chl-a*$^{(2\text{-}Sens)}$ ratios are ~1.1–1.2, indicating the upwelling-induced Chl-a bloom is captured and enhanced in the gap-free *Chl-a*$^{(3\text{-}Sens)}$ image.

Fig. 6d shows *Chl-a*$^{(3\text{-}Sens)}$ of July 15, 2020, in the Gulf of Mexico, where Chl-a features were mainly dominated by the Loop Current (LC) and its associated eddies (Hamilton, 1990). The anticyclonic circulation inside of the LC and its associated eddy was convergent, and thus formed a downwelling warm-core eddy. Within a warm-core eddy, the nutrient supply was poor, and Chl-a were very low (Leterme and Pingree, 2008). In Fig. 6d, there were two warm-core eddies with quite low Chl-a (< ~0.1 mg m^{-3}), which were shredded from the LC. The northern part of the Gulf of Mexico featured a high Chl-a (> ~1.0 mg m^{-3}) associated with the Mississippi River Estuary. In fact, in the region around the Mississippi River Delta, Chl-a are usually quite high (~10 mg m^{-3}). In addition, there are frequent algae blooms on the West Florida Shelf and some of them are harmful. Fig. 6h shows that spatial feature of a high Chl-a (~10 mg m^{-3}) near the Mississippi River Delta and on the West Florida Shelf was further enhanced in the *Chl-a*$^{(3\text{-}Sens)}$ image, compared with those from the *Chl-a*$^{(2\text{-}Sens)}$ image.

To quantitatively compare the *Chl-a*$^{(3\text{-}Sens)}$ and *Chl-a*$^{(2\text{-}Sens)}$ images in coastal oceans, six coastal regions, i.e., the Gulf of Mexico, U.S. East Coast, U.S. West Coast, Brazil Coast, Bay of Bangel, and China East Coast, were selected, and the statistics of ratio and difference between

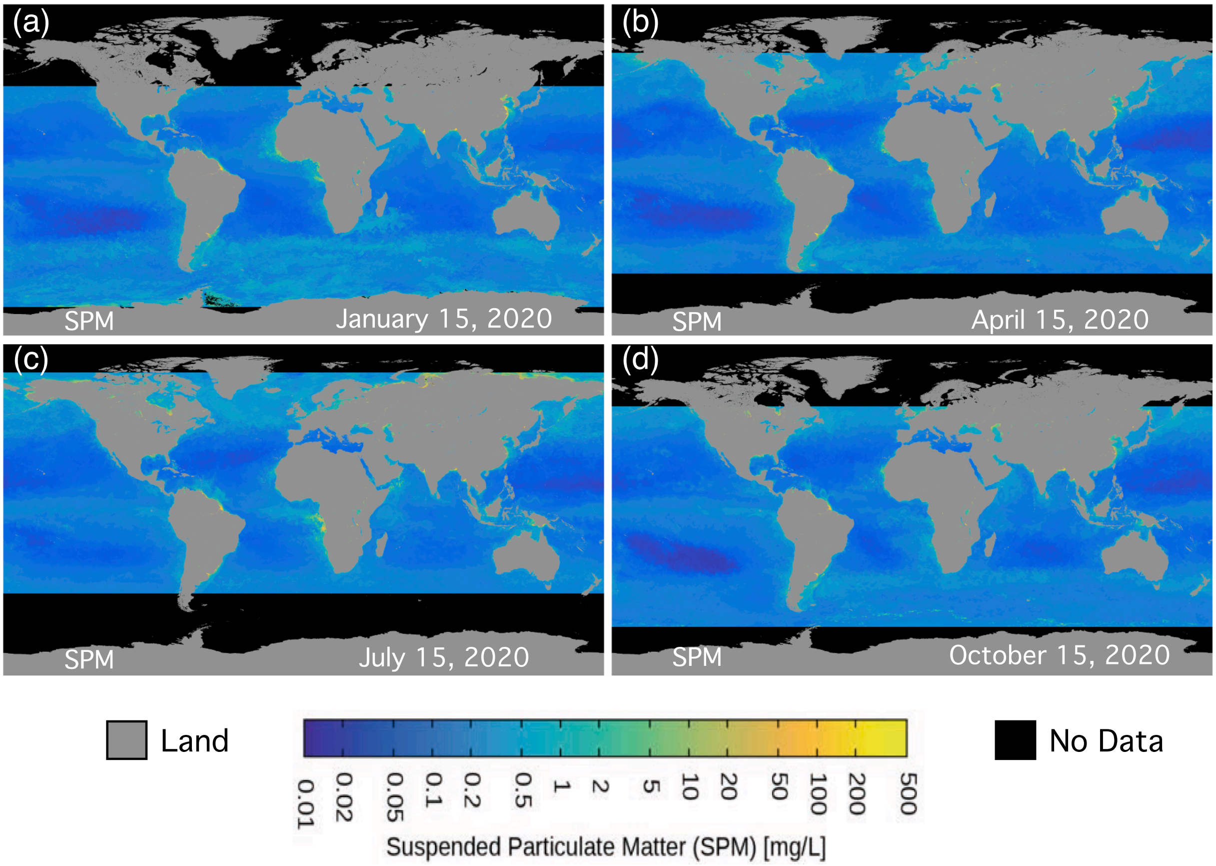

Fig. 9. Global gap-free SPM reconstructed from three sensors (VIIRS-SNPP, VIIRS-NOAA-20, and OLCI-Sentinel-3A) on (a) January 15, (b) April 15, (c) July 15, and (d) October 15, 2020.

$Chl\text{-}a^{(3\text{-}Sens)}$ and $Chl\text{-}a^{(2\text{-}Sens)}$ were computed from the four months of January, April, July, and October in 2020. The statistics results are shown in Table 2. Table 2 shows that the China East Coast has the largest $Chl\text{-}a^{(3\text{-}Sens)}/Chl\text{-}a^{(2\text{-}Sens)}$ mean ratio (1.056), while mean ratios for the Gulf of Mexico, U.S. West Coast, Brazil Coast, and Bay of Bangel are ranging from ~ 0.981–1.02 (within about 2%). The smallest $Chl\text{-}a^{(3\text{-}Sens)}/Chl\text{-}a^{(2\text{-}Sens)}$ ratio is for the U.S. East Coast with mean and median values of 1.008 and 0.999, respectively.

3.2. Gap-free $K_d(490)$ data

Fig. 7 provides examples of the global gap-free $K_d(490)$ images for January 15, April 15, July 15, and October 15 in 2020. Very clear waters with $K_d(490) < \sim 0.05\ \mathrm{m}^{-1}$ were found in the five major ocean basins, i.e., the North and South Pacific, North and South Atlantic, and South Indian Oceans. In the Southern Ocean and high-latitude North Atlantic and Pacific Oceans, ocean waters were moderately turbid ($K_d(490) \sim 0.1\ \mathrm{m}^{-1}$) mainly due to active biological process. The Southern Ocean had the maximum turbidity ($K_d(490) \sim 0.1\ \mathrm{m}^{-1}$) on January 15, 2020 (Fig. 7a), while the high-latitude North Atlantic and Pacific Oceans reached their maximum on July 15, 2020 (Fig. 7c). In addition, some coastal oceans also showed moderate turbidity (e.g., $K_d(490) \sim 0.1\ \mathrm{m}^{-1}$) in different months. For example, waters were turbid along the northwest coast of Africa on January 15 (Fig. 7a), and southwest coast of Africa on July 15 (Fig. 7c). There was also strong turbidity in the Somali Coast on July 15 owing to the monsoon-induced upwelling (Fig. 7c). The East China Sea and Bohai Sea were turbid all year round. The extremely turbid ($K_d(490) > \sim 2.0\ \mathrm{m}^{-1}$) were mainly found in the China East Coast, La Plata River Estuary, Amazon River Estuary, and Southwest Africa Coast.

To quantitively evaluate the global gap-free $K_d(490)$ product, we adopted the same validation procedure that was used to evaluate the global gap-free Chl-a product (Liu and Wang, 2018). Specifically, we randomly selected 5% of the non-missing/valid pixels from the merged data, and purposely set them as "missing pixels," i.e., removed these selected pixels. These pixels were reconstructed by the DINEOF process and validated against the original data. Fig. 8 shows the $K_d(490)$ comparison of the reconstructed data with those from the original in the density scatter plots for the same four days as in Fig. 7. The majority of the data in Fig. 8 are at around 1:1 line in the global ocean with moderate scatter in all four months. Quantitatively, as noted in Fig. 8, the mean ratios of the reconstructed over original data are 1.029, 1.005, 1.030, and 1.002 for the cases of January 15, April 15, July 15, and October 15 in 2020, respectively, with the corresponding STD values of 0.169, 0.142, 0.167, and 0.153, respectively.

It should be noted that the gap-free data are generally smoother than the original ones. This is due to the fact that not all EOF modes are used in the final data reconstruction in the DINEOF procedure, and the original data noise, as well as small scale and transient features in the high order EOF modes, may be removed from the reconstructed data.

3.3. Gap-free SPM data

Fig. 9 provides examples of global gap-free SPM images for January 15, April 15, July 15, and October 15 in 2020. The SPM concentration is closely related to the water turbidity, i.e., high SPM corresponds to a large $K_d(490)$ value, and vice versa. Therefore, the general pattern of the global SPM feature is similar to that of $K_d(490)$. In the Southern Ocean and high latitude Northern Pacific Ocean and Northern Atlantic Ocean, SPM are $\sim 1.0\ \mathrm{mg\ L}^{-1}$, while SPM are low in the major ocean basins and high in the coastal regions. However, SPM data provide more details of ocean/water spatial variation than that from $K_d(490)$ in the world major

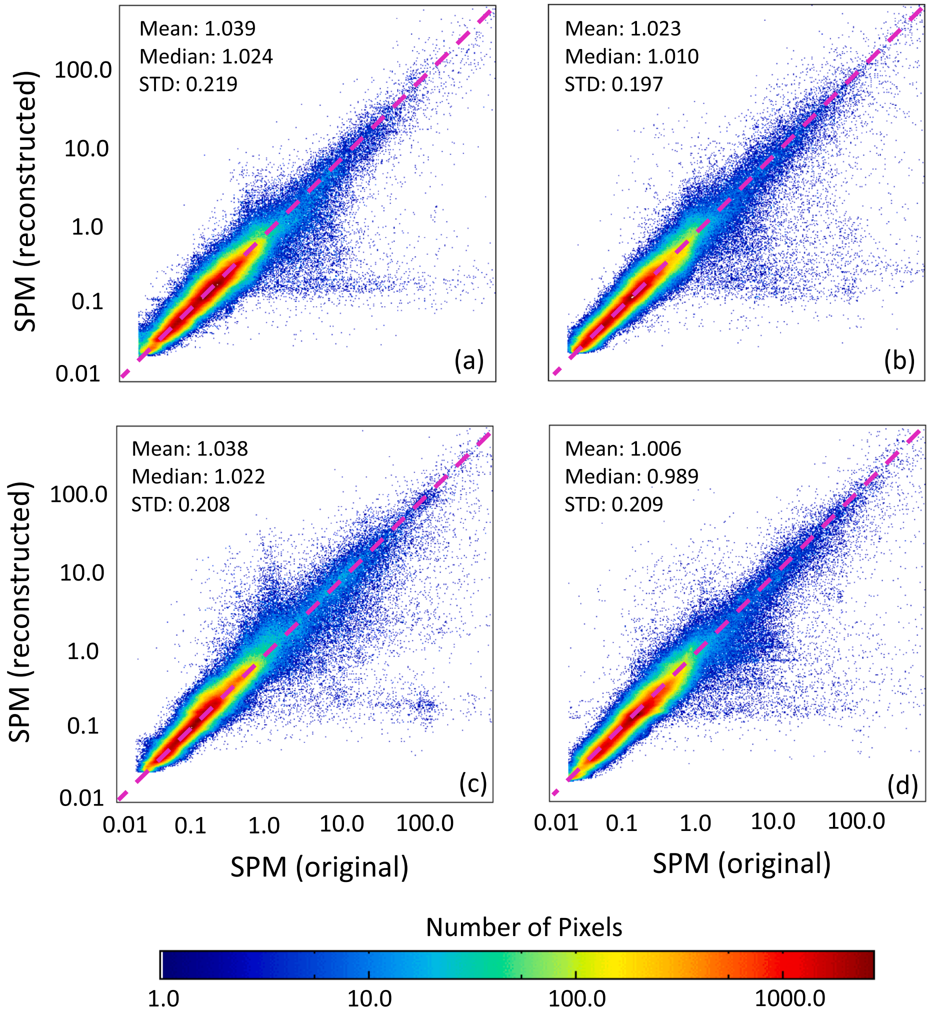

Fig. 10. Density scatter plots of gap-free SPM versus original SPM on (a) January 15, (b) April 15, (c) July 15, and (d) October 15, 2020. Note that SPM unit is mg L^{-1}.

Table 3
Statistics of ratio in (reconstructed/original) and difference (Diff.) in (reconstructed − original) for the months of January, April, July, and October in 2020 for parameters of $K_d(490)$, SPM, and Chl-a. Note that the monthly statistics were calculated from global monthly (daily) data for the specific parameter.

Month (in 2020)		January		April		July		October	
		Ratio	Diff.‡	Ratio	Diff.‡	Ratio	Diff.‡	Ratio	Diff.‡
K_d(490)	Mean	1.013	−0.006	1.010	−0.006	1.019	−0.011	1.009	−0.007
	Median	1.007	0.000	1.006	0.000	1.013	0.000	1.005	0.000
	STD	0.159	0.126	0.144	0.140	0.159	0.227	0.153	0.168
SPM	Mean	1.022	−0.018	1.019	−0.016	1.025	−0.018	1.015	−0.017
	Median	1.004	0.001	1.005	0.000	1.011	0.001	0.999	0.000
	STD	0.216	0.400	0.198	0.444	0.204	0.617	0.203	0.478
Chl-a	Mean	1.015	−0.018	1.014	−0.013	1.020	−0.011	1.013	−0.010
	Median	0.994	0.000	0.996	0.000	1.001	0.001	0.994	0.000
	STD	0.240	0.447	0.210	0.499	0.219	0.720	0.217	0.507

‡ Units for $K_d(490)$, SPM, and Chl-a are m^{-1}, mg L^{-1}, and mg m^{-3}, respectively.

ocean basins. For example, there is a clear area of low SPM (~0.1 mg L^{-1}) in the center of the South Pacific Gyre (Fig. 9a, c, and d), which may not be obviously shown in the gap-free $K_d(490)$ images. In the coastal regions, there is also a broad SPM variation ranging from 0.01 to over 500.0 mg L^{-1}, which provides more details of spatial SPM features from turbid coastal oceans to extremely turbid estuaries (five orders of magnitude in SPM). Fig. 10 shows the comparison of the reconstructed SPM with those from the original in density scatter plots for the same four days as in Fig. 9. Results in Fig. 10 show that the majority of the data are around the 1:1 line in the global oceans with moderate scatter in all the four daily cases (representing four seasons). Quantitatively, as noted in Fig. 10, the mean SPM ratios in the reconstructed/original are 1.039, 1.023, 1.038, and 1.006 for the cases of January 15, April 15, July 15, and October 15 in 2020, respectively, with the corresponding STD values of 0.219, 0.197, 0.208, and 0.209, respectively. In fact, the median ratios are better than the mean ratios with the corresponding values of 1.024, 1.010, 1.022, and 0.989 for these four daily cases (Fig. 10).

In summary, from the daily evaluations (Figs. 8 and 10), the gap-free global K_d(490) and SPM products, derived from the three-sensor merged data, have a similar performance for the reconstructed pixels. To provide more solid evaluations of the three-sensor-derived gap-free Chl-a, K_d(490), and SPM, we have calculated statistics of the ratio between reconstructed and original (i.e., reconstructed/original) and the difference between reconstructed and original (i.e., reconstructed − original) for these three parameters using the entire monthly data of January, April, July, and October in 2020. Table 3 provides these monthly statistics for the three parameters. In fact, for the three products, their performances are quite consistent with the monthly mean ratio varying from 1.009 to 1.025, median ratio from 0.994 to 1.011, and STD from 0.144 to 0.240. Results in Figs. 8, 10, and Table 3 show that global gap-free K_d(490) and SPM products are accurate and reliable, and these data are applicable for various research and applications, particularly over global coastal and inland waters.

4. Discussions and conclusion

Ocean color data from the OLCI-Sentinel-3A are included into the two VIIRS sensors to generate three-sensor merged global Level-3 daily Chl-a, K_d(490), and SPM data, and Level-4 global gap-free daily images are also produced using the DINEOF method. Results show that, by adding the OLCI data, a three-sensor merged daily image has ~11% more valid pixels than a two-sensor merged image. In the global open ocean, the gap-free Chl-a data from three sensors are close to those from two sensors. However, over coastal and inland lake regions, the three-sensor-derived gap-free Chl-a images report noticeably different Chl-a values. Further investigation of some coastal regions (e.g., the La Plata River Estuary, Amazon River Estuary, West Africa Coast, etc.) shows that in the areas of high Chl-a ($> \sim 10$ mg m^{-3}) these spatial features are significantly enhanced using the three-sensor-derived Chl-a images. It is found that the three-sensor reconstructed Chl-a values are ~10–20% higher than those from the two sensors for the pixels of high Chl-a. This is attributed to the new OLCI data as an additional input source. It is emphasized that we are focusing on the enhanced Chl-a spatial features from the three-sensor data. Although excessive nutrient supply from river runoff often stimulates phytoplankton blooms in the estuaries, the sediments and colored dissolved organic matter in the turbid coastal oceans could significantly affect the optical property of the water, and compromises Chl-a accuracy measured from different satellites. Therefore, further validation of the gap-free Chl-a data with in situ data in turbid coastal oceans and estuaries is recommended.

It is also found that the difference between the three-sensor and two-sensor reconstructed gap-free data have seasonal variations. In oligotrophic waters, the three-sensor reconstructed Chl-a data are smaller than those from the two-sensor in April and July, and they are very close in January and October. In global oceans, the three-sensor Chl-a data are generally very close to two-sensor in April and July, while the three-sensor Chl-a data are ~1.5% higher than those from the two-sensor in January and October. The seasonal Chl-a differences between three-sensor and two-sensor reconstructed gap-free data are mainly due to the differences between two-sensor- and three-sensor-merged Chl-a data. Generally, three-sensor merged Chl-a data provide more complete spatial coverage, leading to the improved input data source with the DINEOF method. Therefore, more accurate and reliable gap-filled Chl-a data can be derived with the three-sensor-merged data.

Global gap-free K_d(490) and SPM data are also produced from the three-sensor merged daily Level-3 images. K_d(490) measures the water turbidity/clarity related to light attenuation in the upper water column, while the SPM directly measures the amount of organic and inorganic suspended particles. Since the suspended biogenic particles are dominant in the upper layers of the open ocean, the spatial pattern in K_d(490) and SPM is similar to that of Chl-a over the major ocean basins with low K_d(490) and SPM values. In coastal/inland waters and estuaries, the suspended particles are often from river and land sources, and sediment resuspension. Turbid waters are found in coastal oceans like the East China Sea, West Africa Coast, Somali Coast, while extremely turbid waters (K_d(490) ~ 2.0 m^{-1} and larger) are mainly in the Amazon River Estuary, China East Coast, La Plata River Estuary, and Southwest Africa Coast. Although the spatial pattern of SPM is similar to that of K_d(490) in coastal oceans, SPM data provide a broader range from ~0.01 to 1000 mg L^{-1}, providing more details of SPM spatial features from moderately turbid to extremely turbid coastal and inland lake regions. We compared the reconstructed K_d(490) and SPM data with the original data for validation. It is found that the performance of the gap-free K_d(490) and SPM data is similar to Chl-a. In fact, the mean values of the monthly median ratios in reconstructed/original for Chl-a, K_d(490), and SPM (Table 3) are 0.996, 1.008, and 1.005, respectively, showing high accuracy for the reconstructed gap-free data with the DINEOF method.

Using the three-sensor-merged data, global daily gap-free Chl-a, K_d(490), and SPM products are now being routinely produced. These global water property data will be useful in ocean color science and user communities for various research and applications.

Credit authorship contribution statement

Xiaoming Liu: Conceptualization, Methodology, Validation, Writing – original draft. **Menghua Wang:** Conceptualization, Methodology, Resources, Visualization, Writing – review & editing, Funding acquisition.

Declaration of Competing Interest

The authors declare that they have no known competing financial interests or personal relationships that could have appeared to influence the work reported in this paper.

Acknowledgments

This work was supported by the Joint Polar Satellite System (JPSS) funding. We thank EUMETSAT for providing OLCI-Sentinel-3A mission-long Level-1B data. We thank three anonymous reviewers for their useful comments. The scientific results and conclusions, as well as any views or opinions expressed herein, are those of the author(s) and do not necessarily reflect those of NOAA or the Department of Commerce.

References

Alvera-Azcarate, A., Barth, A., Rixen, M., Beckers, J., 2005. Reconstruction of incomplete oceanographic data sets using Empirical Orthogonal Functions. Application to the Adriatic Sea. Ocean Modeling 9, 325–346.

Barnes, B.B., Cannizzaro, J.P., English, D.C., Hu, C., 2019. Validation of VIIRS and MODIS reflectance data in coastal and oceanic waters: An assessment of methods. Remote Sens. Environ. 220, 110–123.

Beckers, J.M., Rixen, M., 2003. EOF calculations and data filling from incomplete oceanographic data sets. J. Atmos. Ocean Technol. 20 (12), 1839–1856.

Behrenfeld, M.J., Falkowski, P.G., 1997. Photosynthetic rates derived from satellite-based chlorophyll concentration. Limnol. Oceanogr. 42 (1), 1–20.

Boss, E., Behrenfeld, M., 2010. In situ evaluation of the initiation of the North Atlantic phytoplankton bloom. Geophys Res Lett 37 (18), n/a–n/a. https://doi.org/10.1029/2010GL044174.

Campbell, J.W., Blaisdell, J.M., Darzi, M., 1996. Level-3 SeaWiFS data products: spatial and temporal binning. Oceanogr. Lit. Rev. 43, 952.

Choi, J.-K., Park, Y.J., Ahn, J.H., Lim, H.-S., Eom, J., Ryu, J.-H., 2012. GOCI, the world's first geostationary ocean color observation satellite, for the monitoring of temporal variability in coastal water turbidity. J. Geophys. Res. 117 (C9), n/a–n/a. https://doi.org/10.1029/2012JC008046.

Clark, D.K., Gordon, H.R., Voss, K.J., Ge, Y., Broenkow, W., Trees, C., 1997. Validation of atmospheric correction over the ocean. J. Geophys. Res. 102, 17209–17217.

Donlon, C., Berruti, B., Buongiorno, A., Ferreira, M.-H., Femenias, P., Frerick, J., Goryl, P., Klein, U., Laur, H., Mavrocordatos, C., Nieke, J., Rebhan, H., Seitz, B., Stroede, J., Sciarra, R., 2012. The Global Monitoring for Environment and Security (GMES) Sentinel-3 mission. Remote Sens. Environ. 120, 37–57. https://doi.org/10.1016/j.rse.2011.07.024.

Esaias, W.E., Abbott, M.R., Barton, I., Brown, O.B., Campbell, J.W., Carder, K.L., Clark, D.K., Evans, R.H., Hoge, F.E., Gordon, H.R., Balch, W.M., Letelier, R., Minnett, P.J., 1998. An overview of MODIS capabilities for ocean science observations. IEEE Trans. Geosci. Remote Sens. 36 (4), 1250–1265.

Fratantoni, D.M., Glickson, D.A., 2002. North Brazil current ring generation and evolution observed with SeaWiFS. J. Phys. Oceanogr. 32 (3), 1058–1074.

Gill, A.E., 1982. Atmosphere and Ocean Dynamics. Academic Press, New York.

Goldberg, M.D., Kilcoyne, H., Cikanek, H., Mehta, A., 2013. Joint Polar Satellite System: The United States next generation civilian polar-orbiting environmental satellite system. J. Geophys. Res. Atmos. 118 (24), 13,463–13,475. https://doi.org/10.1002/2013JD020389.

Gordon, H.R., Wang, M., 1994. Retrieval of water-leaving radiance and aerosol optical thickness over the oceans with SeaWiFS: A preliminary algorithm. Appl. Opt. 33 (3), 443–452. https://doi.org/10.1364/AO.33.000443.

Gunes, H., Sirisup, S., Karniadakis, G.E., 2006. Gappy data: To Krig or not to Krig? J. Computat. Phys. 212 (1), 358–382. https://doi.org/10.1016/j.jcp.2005.06.023.

Hamilton, P., 1990. Deep Currents in the Gulf of Mexico. J. Phys. Oceanogr. 20 (7), 1087–1104.

Hardman-Mountford, N.J., Richardson, A.J., Agenbag, J.J., Hagen, E., Nykjaer, L., Shillington, F.A., Villacastin, C., 2003. Ocean climate of the South East Atlantic observed from satellite data and wind models. Prog. Oceanogr. 59 (2-3), 181–221.

Henn, B., Raleigh, M.S., Fisher, A., Lundquist, J.D., 2013. A comparison of methods for filling gaps in hourly near-surface air temperature data. J. Hydrometeorol. 14, 929–945.

Hlaing, S., Harmel, T., Gilerson, A., Foster, R., Weidemann, A., Arnone, R., Wang, M., Ahmed, S., 2013. Evaluation of the VIIRS ocean color monitoring performance in coastal regions. Remote Sens. Environ. 139, 398–414.

Hu, C., Barnes, B.B., Feng, L., Wang, M., Jiang, L., 2020. On the interplay between ocean color data quality and data quantity: Impacts of quality control flags. IEEE Geosci. Remote Sens. Lett. 17 (5), 745–749.

Hu, C., Lee, Z., Franz, B.A., 2012. Chlorophyll a algorithms for oligotrophic oceans: A novel approach based on three-band reflectance difference. J. Geophys. Res. 117, C01011, doi: 10.01029/02011JC007395.

Jiang, L., Wang, M., 2013. Identification of pixels with stray light and cloud shadow contaminations in the satellite ocean color data processing. Appl. Opt. 52 (27), 6757–6770. https://doi.org/10.1364/AO.52.006757.

Jiang, L., Wang, M., 2014. Improved near-infrared ocean reflectance correction algorithm for satellite ocean color data processing. Opt. Express 22 (18), 21657–21678. https://doi.org/10.1364/OE.22.021657.

Johns, W.E., Lee, T.N., Schott, F.A., Zantopp, R.J., Evans, R.H., 1990. The North Brazil Current retroflection: Seasonal structure and eddy variability. J. Geophys. Res. Oceans 95, 22103–22120.

Kämpf, J., Chapman, P. (Eds.), Upwelling Systems of the World: A Scientific Journey to the Most Productive Marine Ecosystems. Springer International Publishing, Cham, pp. 251-314.

Leterme, S.C., Pingree, R.D., 2008. The Gulf Stream, rings and North Atlantic eddy structures from remote sensing (Altimeter and SeaWiFS). J. Mar. Syst. 69 (3-4), 177–190.

Liston, G.E., Elder, K., 2006. A meteorological distribution system for high-resolution terrestrial modeling (MicroMet). J. Hydrometeor. 7, 217–234.

Liu, X., Wang, M., 2018. Gap filling of missing data for the VIIRS global ocean color products using the DINEOF method. IEEE Trans. Geosci. Remote Sens. 56, 4464–4476.

Liu, X., Wang, M., 2019. Filling the gaps of missing data in the merged VIIRS SNPP/NOAA-20 ocean color product using the DINEOF method. Remote Sens. 11, 178. https://doi.org/10.3390/rs11020178.

Mikelsons, K., Wang, M., 2019. Optimal satellite orbit configuration for global ocean color product coverage. Opt. Express 27 (8), A445–A457. https://doi.org/10.1364/OE.27.00A445.

Mikelsons, K., Wang, M., Jiang, L., 2020. Statistical evaluation of satellite ocean color data retrievals. Remote Sens. Environ. 237, 111601. https://doi.org/10.1016/j.rse.2019.111601.

Mikelsons, K., Wang, M., Wang, X.-L., Jiang, L., 2021. Global land mask for satellite ocean color remote sensing. Remote Sens. Environ. 257, 112356. https://doi.org/10.1016/j.rse.2021.112356.

Milliman, J.D., Farnsworth, K.L., 2013. River discharge to the coastal ocean: a global synthesis. Cambridge University Press.

Morel, A., Antoine, D., 1994. Heating rate within the upper ocean in relation to its bio-optical state. J. Phys. Oceanogr. 24 (7), 1652–1665.

Mueller, J.L., 2000. SeaWiFS algorithm for the diffuse attenuation coefficient, K(490), using water-leaving radiances at 490 and 555 nm. NASA Goddard Space Flight Center, Greenbelt, Maryland, pp. 24–27.

O'Reilly, J.E., Maritorena, S., Mitchell, B.G., Siegel, D.A., Carder, K.L., Garver, S.A., Kahru, M., McClain, C., 1998. Ocean color chlorophyll algorithms for SeaWiFS. J. Geophys. Res. 103 (C11), 24937–24953.

Ondrusek, M., Lance, V.P., Wang, M., Stengel, E., Kovach, C., Freeman, S., Mannino, A., Gilerson, A., Carrizo, C., Grotsch, P., Herrera, E., Malinowski, M., Ahmed, S., Goes, J. I., Wu, J., Gomes, H., McKee, K., Hu, C., Cannizzaro, J., Zhang, Y., Zhang, Y., English, D., Ladner, S., Goode, W., Lee, Z.P., Wei, J., Shang, Z., Twardowski, M., Stockley, N., Strait, C., Voss, K.J., 2021. Report for Dedicated JPSS VIIRS Ocean Color Calibration/Validation Cruise September 2019. In: Lance, V.P. (Ed.), NOAA Technical Report NESDIS 154. NOAA National Environmental Satellite, Data, and Information Service, Silver Spring, Maryland. https://doi.org/10.25923/p9de-yw97.

Ouillon, S., Douillet, P., Andréfouët, S., 2004. Coupling satellite data with in situ measurements and numerical modeling to study fine suspended-sediment transport: a study for the lagoon of New Caledonia. Coral Reefs 23, 109-122.

Platt, T., Sathyendranath, S., 1988. Oceanic primary production: estimation by remote sensing at local and regional scales. Science 241 (4873), 1613–1620.

Sathyendranath, S., Gouveia, A.D., Shetye, S.R., Ravindran, P., Platt, T., 1991. Biological control of surface temperature in the Arabian Sea. Nature 349 (6304), 54–56.

Shi, W., Wang, M., 2012. Satellite views of the Bohai Sea, Yellow Sea, and East China Sea. Prog. Oceanogr. 104, 35–45. https://doi.org/10.1016/j.pocean.2012.05.001.

Shi, W., Wang, M., 2014. Ocean reflectance spectra at the red, near-infrared, and shortwave infrared from highly turbid waters: A study in the Bohai Sea, Yellow Sea, and East China Sea. Limnol. Oceanogr. 59 (2), 427–444.

Shi, W., Wang, M., 2020. Water properties in the La Plata River Estuary from VIIRS observations. Continent. Shelf Res. 198, 104100. https://doi.org/10.1016/j.csr.2020.104100.

Shi, W., Wang, M., Jiang, L., 2011. Spring-neap tidal effects on satellite ocean color observations in the Bohai Sea, Yellow Sea, and East China Sea. J. Geophys. Res. 116, C12032. https://doi.org/10.1029/2010JC007234.

Siegel, D.A., Doney, S.C., Yoder, J.A., 2002. The North Atlantic spring phytoplankton bloom and sverdrup's critical depth hypothesis. Science 296 (5568), 730–733.

Signorini, S.R., Franz, B.A., McClain, C.R., 2015. Chlorophyll variability in the oligotrophic gyres: mechanisms, seasonality and trends. Front. Mar. Sci 2, 1. https://doi.org/10.3389/fmars.2015.00001.

Son, SeungHyun, Wang, M., 2015. Diffuse attenuation coefficient of the photosynthetically available radiation Kd(PAR) for global open ocean and coastal waters. Remote Sens. Environ. 159, 250–258.

Stahl, K., Moore, R.D., Floyer, J.A., Asplin, M.G., McKendry, I.G., 2006. Comparison of approaches for spatial interpolation of daily air temperature in a large region with complex topography and highly variable station density. Agric. For. Meteorol. 139 (3-4), 224–236.

Stroud, J.R., Lesht, B.M., Schwab, D.J., Beletsky, D., Stein, M.L., 2009. Assimilation of satellite images into a sediment transport model of Lake Michigan. Water Resour. Res. 45 (2) https://doi.org/10.1029/2007WR006747.

Stumpf, R.P., Culver, M.E., Tester, P.A., Kirkpatrick, G.J., Pederson, B., Tomlinson, M.C., Truby, E., Ransibrahmanakul, V., Hughes, K., Soracco, M., 2003. Use of satellite imagery and other data for monitoring *Karenia brevis* blooms in the Gulf of Mexico. Harmful Algae 2, 147–160.

Tomlinson, M.C., Stumpf, R.P., Ransibrahmanakul, V., Truby, E.W., Kirkpatrick, G.J., Pederson, B.A., Vargo, G.A., Heil, C.A., 2004. Evaluation of the use of SeaWiFS imagery for detecting *Karenia Brevis* harmful algal blooms in the eastern Gulf of Mexico. Remote Sens. Environ. 91 (3-4), 293–303.

Wang, M., 2007. Remote sensing of the ocean contributions from ultraviolet to near-infrared using the shortwave infrared bands: simulations. Appl. Opt. 46 (9), 1535–1547. https://doi.org/10.1364/AO.46.001535.

Wang, M., Ahn, J.-H., Jiang, L., Shi, W., Son, SeungHyun, Park, Y.-J., Ryu, J.-H., 2013. Ocean color products from the Korean Geostationary Ocean Color Imager (GOCI). Opt. Express 21 (3), 3835–3849. https://doi.org/10.1364/OE.21.003835.

Wang, M., Isaacman, A., Franz, B.A., McClain, C.R., 2002. Ocean color optical property data derived from the Japanese Ocean Color and Temperature Scanner and the French Polarization and Directionality of the Earth's Reflectances: A comparison study. Appl. Opt. 41 (6), 974–990. https://doi.org/10.1364/AO.41.000974.

Wang, M., Jiang, L., Mikelsons, K., Liu, X., 2021. Satellite-derived global chlorophyll-a anomaly products. Int. J. Appl. Earth Obs. Geoinf. 97, 102288. https://doi.org/10.1016/j.jag.2020.102288.

Wang, M., Jiang, L., Son, SeungHyun, Liu, X., Voss, K.J., 2020a. Deriving consistent ocean biological and biogeochemical products from multiple satellite ocean color sensors. Opt. Express 28 (3), 2661–2682. https://doi.org/10.1364/OE.376238.

Wang, M., Shi, W., 2007. The NIR-SWIR combined atmospheric correction approach for MODIS ocean color data processing. Opt. Express 15 (24), 15722–15733. https://doi.org/10.1364/OE.15.015722.

Wang, M., Shi, W., Watanabe, S., 2020b. Satellite-measured water properties in high altitude Lake Tahoe. Water Res. 178, 115839. https://doi.org/10.1016/j.watres.2020.115839.

Wang, M., Son, SeungHyun, 2016. VIIRS-derived chlorophyll-a using the ocean color index method. Remote Sens. Environ. 182, 141–149.

Wang, M., Son, S., Harding, L.W., J.,, 2009. Retrieval of diffuse attenuation coefficient in the Chesapeake Bay and turbid ocean regions for satellite ocean color applications. J. Geophys. Res. 114, C10011. https://doi.org/10.1029/2009JC005286.

Wei, J., Wang, M., Jiang, L., Yu, X., Mikelsons, K., Shen, F., 2021. Global estimation of suspended particulate matter from satellite ocean color imagery. J. Geophys. Res. Oceans 126, e2021JC017303, 10.1029/2021JC017303.

Yang, H., Choi, J.-K., Park, Y.-J., Han, H.-J., Ryu, J.-H., 2014. Application of the Geostationary Ocean Color Imager (GOCI) to estimates of ocean surface currents. J. Geophys. Res. Oceans 119 (6), 3988–4000.

Yu, X., Lee, Z., Shen, F., Wang, M., Wei, J., Jiang, L., Shang, Z., 2019. An empirical algorithm to seamlessly retrieve the concentration of suspended particulate matter from water color across ocean to turbid river mouths. Remote Sens. Environ. 235, 111491. https://doi.org/10.1016/j.rse.2019.111491.